CHEMISTRY OF MATERIALS

Article

pubs.acs.org/cm

In Situ Time-Resolved Attenuated Total Reflectance Infrared Spectroscopy for Probing Metal–Organic Framework Thin Film Growth

Junjie Zhao,[†,‡] Berc Kalanyan,[*,‡] Heather F. Barton,[†] Brent A. Sperling,[‡] and Gregory N. Parsons[*,†]

[†]Department of Chemical & Biomolecular Engineering, North Carolina State University, 911 Partners Way Campus, Box 7905, Raleigh, North Carolina 27695, United States

[‡]National Institute of Standards and Technology (NIST), Gaithersburg, Maryland 20899, United States

Supporting Information

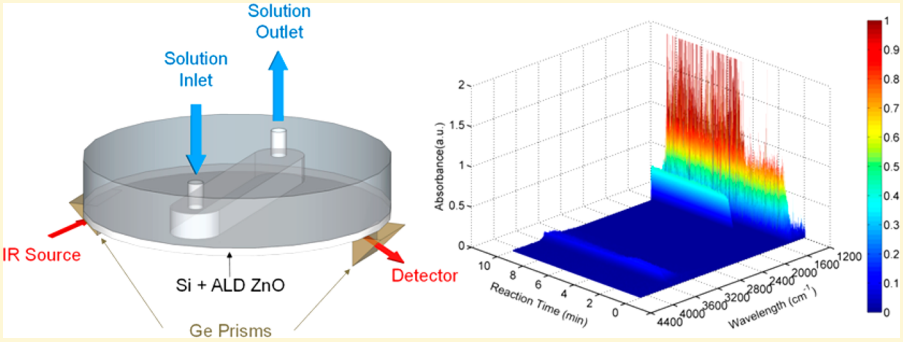

ABSTRACT: *In situ* chemical measurements of solution/surface reactions during metal–organic framework (MOF) thin film growth can provide valuable information about the mechanistic and kinetic aspects of key reaction steps and allow control over crystal quality and material properties. Here, we report a new approach to studying the growth of MOF thin films in a flow cell using attenuated total reflectance Fourier transform infrared spectroscopy (ATR-FTIR). Real-time spectra recorded during continuous-flow synthesis were used to investigate the mechanism and kinetics that govern the formation of (Zn,Cu) hydroxy double salts (HDSs) from ZnO thin films and the subsequent conversion of HDS to HKUST-1. We found that both reactions follow pseudo-first-order kinetics. Real-time measurements also revealed that the limited mass transport of reactants may lead to partial conversion of ZnO to HDS and therefore leaves an interfacial ZnO layer beneath the HDS film, providing strong adhesion of the HKUST-1 coating to the substrate. This *in situ* flow-cell ATR-FTIR method is generalizable for studying the dynamic processes of MOF thin film growth and could be used for other solid/liquid reaction systems involving thin films.

INTRODUCTION

With their intrinsic porosity and a diversity of crystalline structures, metal–organic frameworks (MOFs) have attracted tremendous interest in the past few decades.[1,2] More than 20000 MOF structures have been reported,[1] and these materials have been investigated for a wide array of applications, such as gas adsorption, separations, and catalysis.[3−7] However, because of the difficulty in probing crystal growth in solutions,[8] obtaining direct evidence to elucidate MOF growth mechanisms continues to be a challenge.[9] As a result, dynamic processes that take place during MOF formation are still not well understood, and MOF synthesis often relies on trial and error.[8] Understanding the mechanism of MOF nucleation and growth will enhance control over the material properties, morphology, and defects[10] and allow the discovery of improved synthesis methods.[9]

Several *in situ* measurements have been previously reported to study how MOFs form, including atomic force microscopy (AFM),[10,11] surface plasmon resonance (SPR) spectroscopy,[12] quartz crystal microbalance (QCM),[13] X-ray diffraction (XRD),[14,15] small-angle and wide-angle X-ray scattering (SAXS and WAXS, respectively),[16−18] and liquid-cell transmission electron microscopy (LCTEM).[19] Attfield et al. probed the surfaces of MOF crystals using *in situ* AFM during the growth of HKUST-1 and MOF-5.[10,11] With subnanometer resolution, this technique can track the growth of crystal surfaces and identify defects present during crystallization. *In situ* SPR and QCM are powerful tools for analyzing the kinetics of the formation of surface-mounted MOFs in real time.[12,13] *In situ* XRD, SAXS, and WAXS have been used to follow the transition of crystal structures during MOF synthesis and to identify intermediate phases.[14−18] Recently, Patterson et al. captured the dynamic processes during ZIF-8 growth using

Received: July 26, 2017
Revised: September 19, 2017
Published: September 21, 2017

DOI: 10.1021/acs.chemmater.7b03096
Chem. Mater. XXXX, XXX, XXX−XXX

LCTEM, providing direct visual evidence of ZIF-8 formation from small constituents.[19]

While previous *in situ* methods have been mainly focused on the changes in the crystal structure, crystal morphology, crystal size, and mass uptake on surfaces, these measurements do not directly reveal chemical information such as bond formation and ion−ligand exchange during the process of MOF growth. Here, we report for the first time the use of *in situ* time-resolved attenuated total reflectance Fourier transform infrared (ATR-FTIR) spectroscopy in a continuous-flow reactor to study the mechanism and kinetics of MOF growth. The ATR technique relies on the total reflection of the IR beam in an internal reflection element (IRE), where surface enhancement is achieved by the evanescent wave formed perpendicular to the reflecting surface in the IRE.[20,21] Compared to transmission FTIR spectroscopy, ATR-FTIR is advantageous for probing surfaces (rather than measuring the bulk) and particularly powerful for *in situ* analyses of chemisorption and reactions at solid−liquid interfaces when the liquid is strongly absorbing.[21] Although liquid-cell ATR measurements are commonly employed for the investigation of a wide variety of molecular adsorption and surface reactions,[22−28] ATR-FTIR has not yet been explored for real-time monitoring of MOF growth.

Key challenges of using ATR-FTIR to study MOF growth are (i) the limited penetration depth of the evanescent wave to probe through the reagent solution and (ii) the lack of controlled MOF nucleation and growth on the IRE. For example, during common solvothermal syntheses, MOF crystals formed in the solution are often observed to fall onto the bottom of the reaction vessel. Consequently, it is difficult to distinguish between homogeneous nucleation (in the solution) and heterogeneous nucleation (on the IRE surface). Once the IRE is covered with a sufficiently thick layer (>1 μm thick) of MOF crystals, the ATR configuration will no longer be able to probe the extent of reaction. After the IRE surface is overcoated with MOFs, it needs to be cleaned or replaced to perform additional measurements.

To deal with these challenges, we designed an ATR configuration to use 50 mm diameter Si wafers as the IRE as shown in Figure 1a (a detailed description of the ATR-FTIR setup is provided in Figure S1). This approach is advantageous because Si wafers are replaceable and less costly than common IREs (e.g., trapezoidal prisms and other geometries). As a test case for our measurement, we focus on the recently reported processes that show controlled MOF nucleation and growth on or from surface metal oxides.[29−36] We use atomic layer deposition (ALD) to prepare a metal oxide thin film on the Si wafer IRE as the starting material or nucleation layer for MOF growth (Figure 1b). In this work, we will use our custom-built flow-cell ATR-FTIR to study the mechanism and kinetics of a recently reported conversion of hydroxy double salt (HDS) to MOFs.[33] In this two-step scheme, ZnO reacts with $Cu(NO_3)_2$ in solution to form (Zn,Cu) hydroxy nitrate, and this HDS intermediate is further converted to the HKUST-1 MOF via anion exchange at room temperature within 1 min (Figure 1c). Previous work also confirms that this approach is generally applicable to other systems, including, for example, Cu-BDC, IRMOF-3, ZIF-8, and other MOF materials.[33] *Ex situ* characterization has been used in the previous report to investigate the reaction mechanism.[33] Here, we show that *in situ* flow-cell ATR-FTIR can capture the dynamics of HDS formation and subsequent anion exchange in the HDS layer that ultimately leads to MOF formation.

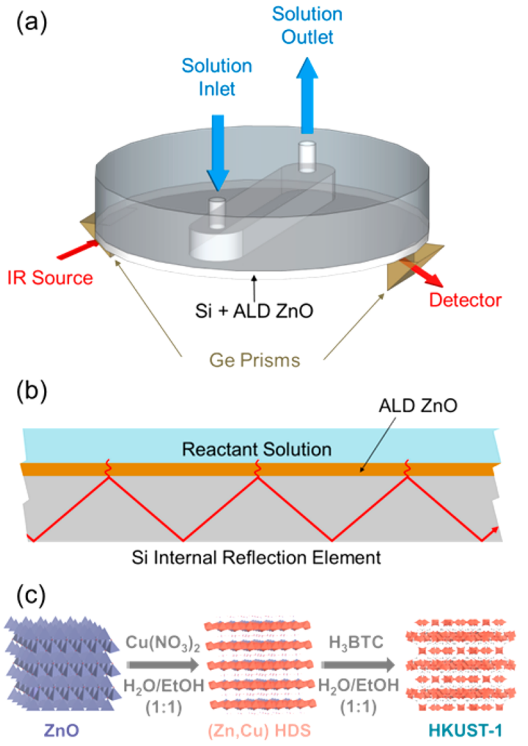

Figure 1. (a) Schematic of the *in situ* ATR-FTIR spectroscopy setup equipped with a liquid flow cell. An undoped silicon wafer is used as the internal reflection element. (b) Schematic of the solid−liquid interface for the surface reactions to form MOF thin films. (c) A layer of ZnO deposited on Si using ALD is used as a templating material for rapid room-temperature synthesis of the HKUST-1 thin film.

RESULTS AND DISCUSSION

We deposited 300 cycles of ALD ZnO (≈60 nm thickness) on the Si wafer as the initiation layer for HDS formation. In a typical room-temperature flow synthesis experiment, a 300 mmol/L $Cu(NO_3)_2$ solution in ethanol and water (ethanol volume fraction of 0.5) was first pumped into the liquid cell for 120 s, followed by a rinse step using the mixed solvent for 60 s. Subsequently, a 10 mmol/L 1,3,5-benzenetricarboxylic acid (H_3BTC) solution in ethanol and water was pumped into the cell for 300 s. After the flow of the H_3BTC solution, the cell was further rinsed with the ethanol/water solvent mixture for 120 s. The flow rate was controlled at 100 mL/min during the entire process. We modified the previously published procedure[33] to exclude dimethylformamide (DMF) from the solvent mixture, because the strong carbonyl band in DMF at ≈1680 cm^{-1} was found to overlap with the asymmetric stretching mode for the carboxylate groups [$\nu_{as}(OCO^-)$] in HKUST-1. Infrared absorbance spectra were recorded every 0.49 s, and each spectrum was referenced against the steady-state flow of the solvent mixture in the absence of reactants. Sets of spectra were analyzed by integrating the peaks for $\nu(NO_3^-)$ at ≈1420 cm^{-1}, $\nu(C{=}C)$ at ≈1588 cm^{-1}, and $\nu_{as}(OCO^-)$ at ≈1647 cm^{-1}.[33] We used peak areas to follow the extent of reaction during HDS formation from ALD ZnO as well as conversion of HDS to HKUST-1.

Figure 2a shows time-resolved ATR-FTIR spectra for the surface reactions to form HKUST-1 thin films (the corresponding three-dimensional plot is shown in Figure S2). Two broad peaks at ≈1360 and ≈1420 cm^{-1} appear after the ZnO-coated IRE is exposed to a $Cu(NO_3)_2$ solution in the flow

DOI: 10.1021/acs.chemmater.7b03096
Chem. Mater. XXXX, XXX, XXX−XXX

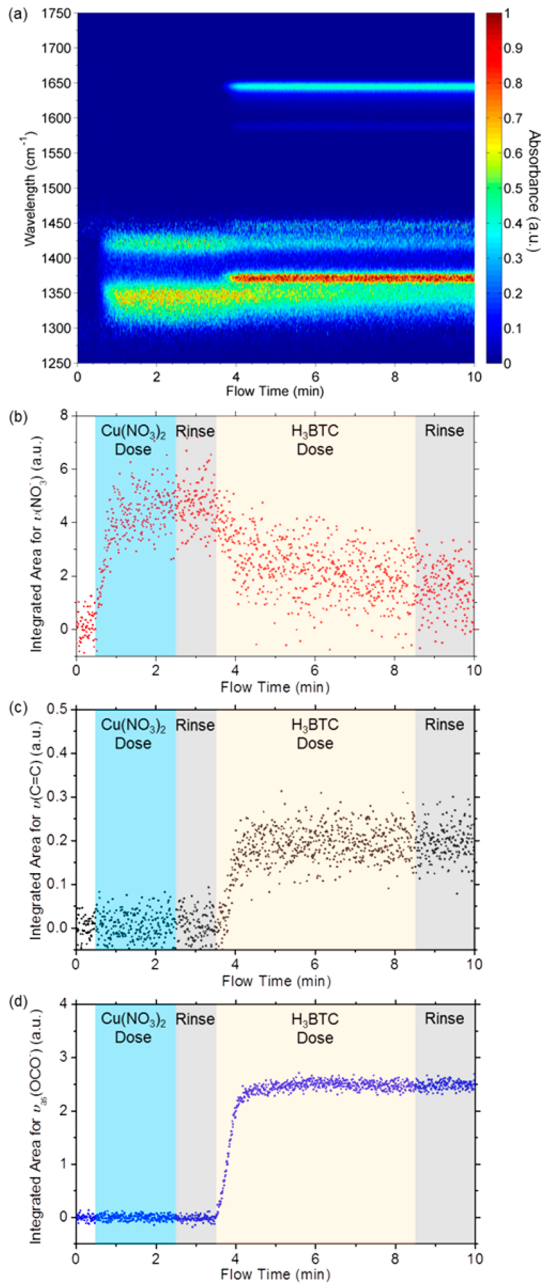

Figure 2. (a) Time-resolved ATR-FTIR spectra for surface reactions to form HKUST-1 thin films. (b–d) Integrated areas for IR peaks representing $\nu(NO_3^-)$ at ≈1420 cm^{-1}, ν(C=C) at ≈1588 cm^{-1}, and $\nu_{as}(OCO^-)$ at ≈1647 cm^{-1}.

cell. These two peaks are associated with vibrations of the NO_3^- groups mainly present in the (Zn,Cu) hydroxy nitrate double salt.[33] The integrated peak area for $\nu(NO_3^-)$ at ≈1420 cm^{-1} (Figure 2b) increases dramatically and reaches saturation after 1 min, indicating the fast formation of (Zn,Cu) HDS from the ZnO thin film. Following the exposure of the ZnO surface to a $Cu(NO_3)_2$ solution, the ethanol/water solvent mixture was used to rinse the cell for 1 min. The absorbance of the $\nu(NO_3^-)$ peaks remains constant during the rinse step. When the H_3BTC solution is dosed into the flow cell at ≈3.5 min, four peaks appear (Figure 2a), which represent the symmetric and asymmetric stretching modes (1378 and 1647 cm^{-1}, respectively) of the carboxylate groups in HKUST-1[33] and the C=C vibration modes (1450 and 1588 cm^{-1}) associated with the aromatic ring in BTC^{3-}. The decreased peak area of $\nu(NO_3^-)$ and the increased peak areas of $\nu_{as}(OCO^-)$ and ν(C=C) were observed simultaneously (Figure 2b–d), consistent with the anion exchange process reported for conversion of HDS to MOFs.[33] The $\nu_{as}(OCO^-)$ and ν(C=C) peaks reach their maximum area within 1 min, showing the rapid conversion of HDS to HKUST-1. Scanning electron microscopy (SEM) images and X-ray diffraction (XRD) patterns in the Figures S3 and S4 confirm that the film formed on the surface is the HKUST-1 MOF with crystal sizes of 571 ± 124 nm.

Because the flow-cell ATR-FTIR measurement can follow the extent of surface reactions, we investigated the kinetics for the formation of HDS from ZnO and the conversion of HDS to HKUST-1. Figure 3a shows the change in the integrated IR

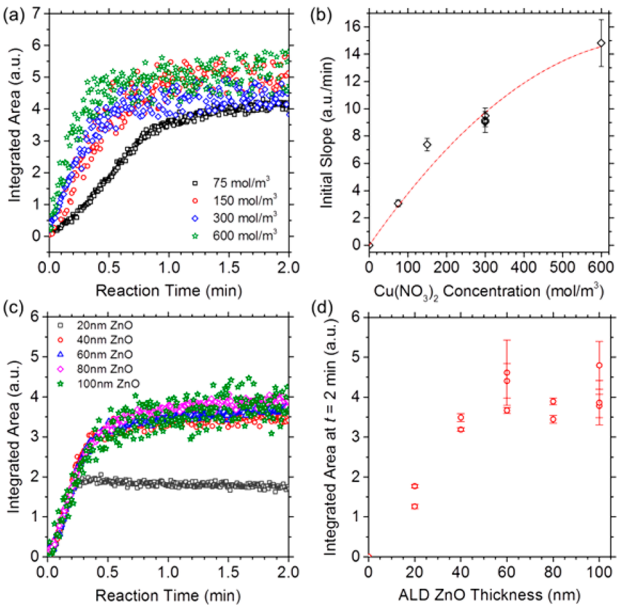

Figure 3. (a) Integrated IR peak area for $\nu(NO_3^-)$ at ≈1420 cm^{-1} as a function of reaction time during the flow of $Cu(NO_3)_2$ solutions with different concentrations (75–600 mmol/L) on a fixed thickness of ALD ZnO (≈60 nm). (b) Initial slope ($0 \le t \le 0.1$ min) derived from the curves in panel a. The dashed curve represents the fit to eq 5. (c) Integrated $\nu(NO_3^-)$ peak area during the flow of 300 mmol/L $Cu(NO_3)_2$ on different thicknesses of ALD ZnO layers (≈20–100 nm). (d) Integrated $\nu(NO_3^-)$ peak area after HDS growth saturation (t = 2.0 min). Error bars in panels b and d represent the standard deviation for each sample.

peak area for $\nu(NO_3^-)$ at ≈1420 cm^{-1} as a function of reaction time when the initial ZnO layer (≈60 nm) is reacted with different concentrations of a $Cu(NO_3)_2$ solution. For all concentrations tested for this reaction, the $\nu(NO_3^-)$ peak area rises rapidly in the first 30 s of reaction and then slowly saturates as the reaction reaches steady-state conditions. To correlate the IR absorbance (A) with the concentration of nitrate groups, we derived eq 1 (full derivation provided in the Supporting Information) on the basis of the differential form of the Beer–Lambert law and the exponential decay of the electric field strength for the evanescent wave.

$$A = \frac{N\alpha}{\ln 10}\left[\frac{C_{N,Sol}}{2\gamma} + (C_{N,HDS} - C_{N,Sol})L_{HDS}\right] \quad (1)$$

DOI: 10.1021/acs.chemmater.7b03096
Chem. Mater. XXXX, XXX, XXX–XXX

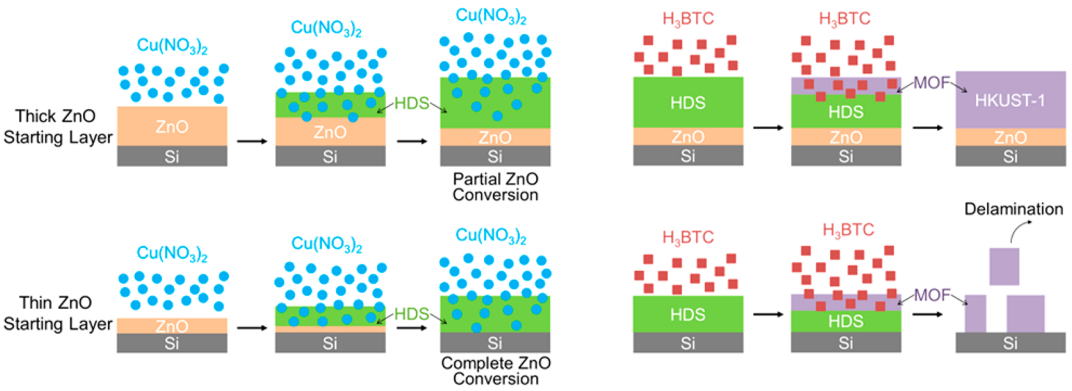

Figure 4. Schematic illustration of the reaction and diffusion processes for thick and thin ZnO starting layers during the formation of HDS and its subsequent conversion to HKUST-1.

where N is the number of total reflections and $C_{N,HDS}$ and $C_{N,Sol}$ (in units of millimoles per liter) are the concentrations of nitrate groups in the HDS film and in the solution, respectively. $C_{N,HDS}$ and $C_{N,Sol}$ are both considered constant during the initial period of reaction. L_{HDS} is the film thickness of (Zn,Cu) HDS, and α and γ are defined in eqs 2 and 3, respectively.

$$\alpha = \varepsilon I_0 e^{-2\gamma d_{ZnO}} \tag{2}$$

where ε is the molar attenuation coefficient for the nitrate groups (in units of square meters per mole), I_0 is the intensity of the incident evanescent wave at the IRE surface, and d_{ZnO} is the distance from the IRE surface to the top surface of the ZnO film. γ is defined as the reciprocal of the penetration depth (d_p) and depends on the refractive indices of the IRE (n_1) and the thin film on top of the IRE (n_2), the angle of incidence (θ), and the IR wavelength (λ).[37,38]

$$\gamma = \frac{1}{d_p} = \frac{2\pi n_1 \sqrt{\sin^2\theta - \left(\frac{n_2}{n_1}\right)^2}}{\lambda} \tag{3}$$

The chemical reactions possibly involved in the process to form HDS from ZnO are written as reactions I and II.

$$ZnO + 2H^+ \rightarrow Zn^{2+} + H_2O \tag{I}$$

$$Zn^{2+} + xCu^{2+} + (y+z)H_2O + (2+2x-y)NO_3^- \rightleftharpoons ZnCu_x(OH)_y(NO_3)_{2+2x-y}\cdot zH_2O + yH^+ \tag{II}$$

Because identifying the elementary reactions and determining a rate-limiting step are nontrivial, we assume that the entire conversion process from ZnO to HDS follows pseudo-first-order kinetics (eq 4).

$$-r_1 = k_{app}C_{Cu} \tag{4}$$

where r_1 is the reaction rate for the overall reaction process, k_{app} is the apparent first-order rate constant, and C_{Cu} is the concentration of Cu^{2+}. Equation 1 then becomes

$$A = \frac{N\alpha}{\ln 10} \times \frac{C_{N,Sol}}{2\gamma} + \frac{(C_{N,HDS} - C_{N,Sol})C_{Cu}}{C_{N,HDS}} \times \varphi t \tag{5}$$

where t is the reaction time (in units of minutes). The grouped kinetic parameter φ is given as

$$\varphi = \frac{N\alpha}{\ln 10} \times \frac{k_{app}V}{S} \tag{6}$$

where V (cubic meters) is the volume of the $Cu(NO_3)_2$ solution involved in the reaction to form the HDS and S (square meters) is the geometric area of the HDS film, i.e., the planar surface area on the wafer exposed to reactants.

As indicated in eq 5, absorbance is linearly related to reaction time. This allows us to interpret the initial slope ($0 \le t \le 0.1$ min) of the curves in Figure 3a as an indication of reaction rate. Figure 3b shows that the initial slope increases with $Cu(NO_3)_2$ concentration. Upon fitting the data with eq 5, we find that the experimental results agree well with the model, confirming that the ZnO-to-HDS conversion can be described by pseudo-first-order kinetics. Fitting of the initial slope using eq 7 gives a φ of 0.041 ± 0.004 m^3 mol^{-1} min^{-1}.

$$\text{initial slope} = \frac{(C_{N,HDS} - C_{N,Sol})C_{Cu}}{C_{N,HDS}} \times \varphi \tag{7}$$

We also studied the effect of the starting thickness of the ZnO films on the kinetics of HDS formation. Figure 3c shows the integrated $\nu(NO_3^-)$ peak area during the flow of 300 mmol/L $Cu(NO_3)_2$ solutions on different thicknesses of ALD ZnO layers (100−500 cycles, ≈20−100 nm). As expected, the initial slopes of the curves in Figure 3c are comparable for all oxide thicknesses tested. To compare the amount of HDS formed at the end of the $Cu(NO_3)_2$ flow, we plotted the final integrated $\nu(NO_3^-)$ peak area at 2 min as a function of the thicknesses of the ZnO films deposited on the Si IRE (Figure 3d). While the $\nu(NO_3^-)$ peak area shows a dependence on the initial ZnO thickness, for ≥60 nm thick ZnO films, the $\nu(NO_3^-)$ peak area exhibits saturation. We calculated the d_p of the ATR evanescent wave on the basis of eq 3 and compared this value with the HDS film thicknesses measured from cross sectional SEM images. In the wavenumber range (1250−1750 cm^{-1}) used to track the reaction that forms (Zn,Cu) HDS from ZnO, d_p ranges from 0.62 to 0.88 μm. These d_p values are larger than the thickest HDS layer (0.56 μm) converted from ≈100 nm thick ALD ZnO (Figure S5), confirming that surface changes during the ZnO-to-HDS conversion are within the information depth of the ATR-FTIR measurement. Transmission IR measurements also indicate that the film thicknesses of the HDS converted from thick ZnO layers (≥60 nm) are indeed very similar (Figure S6). These results reveal that full conversion is not achieved for thick ZnO starting layers during flow synthesis.

DOI: 10.1021/acs.chemmater.7b03096
Chem. Mater. XXXX, XXX, XXX−XXX

The partial conversion of thick ZnO layers to (Zn,Cu) HDS possibly stems from a diffusion-limited process. As shown in Figure 3c, for ZnO initial layers with thicknesses of ≥60 nm, the increase in the $\nu(NO_3^-)$ peak area stops after 0.5 min. The dense HDS formed on the surface may impede the diffusion of the reactant into the film, thus hindering mass transport (Figure 4). Consequently, the growth of HDS stops at a certain depth where the reactant is either depleted or at a low concentration, leaving an interfacial layer of ZnO between the HDS film and the Si substrate. The XRD results in Figure S4 also confirm the existence of ZnO in the HDS films synthesized from thick ZnO initiation layers.

We observed that the ZnO interfacial layer due to partial conversion to HDS plays a critical role in attaching the MOF thin films to the substrate during the conversion of as-synthesized (Zn,Cu) HDS to HKUST-1 films (Figure 4). To demonstrate this, we studied the formation of HKUST-1 films using a 10 mmol/L H_3BTC solution and HDS prepared from ZnO initial films with different thicknesses. Time-resolved IR spectra confirm the formation of HKUST-1 from (Zn,Cu) HDS regardless of the thickness of the ZnO initial layers (Figure S7). In cases in which a ZnO interfacial layer remained beneath the MOF films (for ZnO thicknesses of ≥60 nm), dense and uniform HKUST-1 films were obtained and found to be attached to the substrate as shown in the SEM images in Figure S8. In comparison, when a thin ZnO initial layer was used, the complete consumption of the ZnO film and the subsequent conversion of HDS to MOF resulted in the delamination and loss of the MOF layer.

We further investigated the kinetics for the conversion of (Zn,Cu) HDS to HKUST-1 by monitoring the $\nu_{as}(OCO^-)$ peak at ≈1647 cm^{-1}. HDS thin films with and without ZnO interfacial layers were synthesized from ≈60 and ≈20 nm thick ALD ZnO films, respectively. The concentration of the H_3BTC solution used in the experiments ranged from 1 to 20 mmol/L. Figure 5a shows the formation of HKUST-1 from HDS in the presence of a ZnO interfacial layer. The area of the $\nu_{as}(OCO^-)$ peak increases dramatically and then reaches a plateau, which indicates maximum conversion of HDS. In comparison, the peak area of $\nu_{as}(OCO^-)$ shown in Figure 5b decreases after the initial growth, indicating film delamination and loss during reactant flow in the cases without the ZnO interfacial layers. Indeed, we observed sparse islands of HKUST-1 crystals on these substrates by SEM (Figure S8).

The reaction associated with the HDS-to-MOF conversion is given in reaction III.

$$\mathrm{ZnCu}_x(\mathrm{OH})_y(\mathrm{NO}_3)_{2+2x-y}\cdot z\mathrm{H}_2\mathrm{O} + \frac{2x}{3}\mathrm{H}_3\mathrm{BTC} \rightarrow \frac{x}{3}\mathrm{Cu}_3\mathrm{BTC}_2\cdot n\mathrm{H}_2\mathrm{O} + \mathrm{Zn}^{2+} + (2x-y)\mathrm{H}^+ + (2+2x-y)\mathrm{NO}_3^- + \left(2x-y+z-\frac{nx}{3}\right)\mathrm{H}_2\mathrm{O} \quad \text{(III)}$$

With a derivation similar to eq 1 and maintaining the assumption of pseudo-first-order kinetics, we obtain eq 8 (full derivation provided in the Supporting Information) to correlate absorbance A' for $\nu_{as}(OCO^-)$ with reaction time.

$$A' = \varphi' C_{BTC} t \quad (8)$$

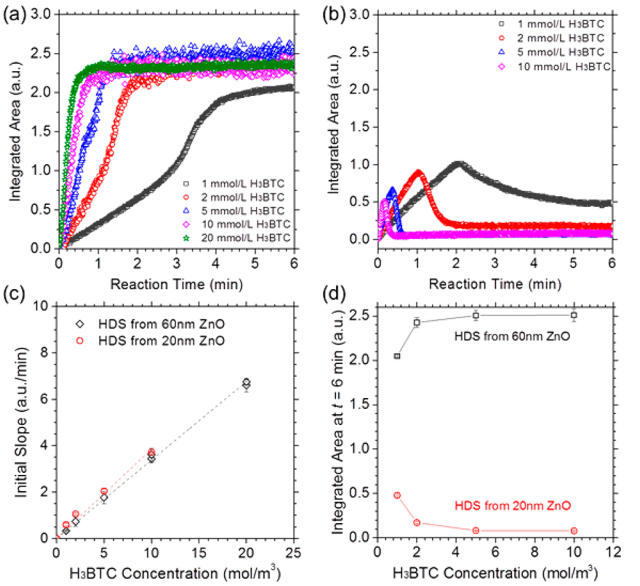

Figure 5. (a and b) Integrated IR peak areas for $\nu_{as}(OCO^-)$ at ≈1647 cm^{-1} as a function of reaction time during the flow of H_3BTC solutions on (Zn,Cu) HDSs converted from (a) ≈60 nm and (b) ≈20 nm ALD ZnO thin films. (c) Initial slope ($0 \le t \le 0.1$ min) derived from the curves in panels a and b as a function of H_3BTC concentration. The dashed line represents linear fitting. (d) Integrated IR peak area for $\nu_{as}(OCO^-)$ at ≈1647 cm^{-1} at 6 min, representing the final amount of HKUST-1 synthesized from HDS thin films with and without a ZnO interfacial layer. Error bars in panels c and d represent the standard deviation for each sample.

where the grouped kinetic parameter φ' for the HDS-to-MOF conversion is defined in eq 9. C_{BTC} is the concentration of H_3BTC in the solution.

$$\varphi' = \frac{N\alpha'}{\ln 10}\frac{k'_{app}V'}{S'} \quad (9)$$

where α', k'_{app}, V', and S' are similar to their counterparts in eqs 2–4 and defined in the Supporting Information.

Equation 8 establishes a linear relationship between absorbance and reaction time, so we can use the initial slope of the integrated $\nu_{as}(OCO^-)$ curve to obtain φ'. The initial slope ($0 \le t \le 0.1$ min) obtained from the curves in panels a and b of Figure 5 exhibits a linear dependence on H_3BTC concentration (Figure 5c). This is consistent with our model and confirms that the conversion of HDS to HKUST-1 is also described by pseudo-first-order kinetics. φ' obtained from linear fitting gives a value of 0.338 ± 0.004 $m^3\ mol^{-1}\ min^{-1}$ for the initial reaction on HDS layers synthesized from ≈60 nm thick ZnO and 0.385 ± 0.017 $m^3\ mol^{-1}\ min^{-1}$ for initial MOF formation on HDS converted from ≈20 nm thick ZnO films. The difference between these two φ' values could be a result of different evanescent wave intensities at the top surfaces of thick and thin HDS films (eq S4).

Figure 5d shows the integrated area for the $\nu_{as}(OCO^-)$ peak after the termination of H_3BTC flow, which represents the total amount of HKUST-1 remaining on the IRE surface. For HDS films obtained from ≈60 nm thick ZnO, the as-synthesized MOF layers were all found to be attached to the substrate regardless of the H_3BTC concentration. Moreover, the integrated $\nu_{as}(OCO^-)$ area increases as a function of H_3BTC concentration. Compared with other concentrations tested, 1 mmol/L H_3BTC results in a notably lower conversion of the

DOI: 10.1021/acs.chemmater.7b03096
Chem. Mater. XXXX, XXX, XXX−XXX

HDS layer synthesized from ≈60 nm thick ZnO, perhaps because the mass transport rate for H_3BTC to diffuse into the HDS film is low due to the relatively small concentration gradient, while the reaction rate to form HKUST-1 with 1 mmol/L H_3BTC is high. The diffusion of H_3BTC in the HKUST-1 growth front could be a secondary factor affecting HDS conversion, depending on the relative diffusivities of H_3BTC in HDS and HKUST-1, respectively. Consequently, the diffusion-controlled process leads to limited conversion of the HDS film.

For HDS films grown from a thin ZnO layer (≈20 nm), the final integrated $\nu_{as}(OCO^-)$ area for the reaction run with 1 mmol/L H_3BTC is significantly larger than for reactions run with ≥2 mmol/L H_3BTC (Figure 5d). The lower effective conversion at increasing H_3BTC concentrations can be explained by rapid delamination of the MOF layer. Therefore, when the H_3BTC concentration is high and the starting ZnO layer is relatively thin, the reaction front quickly reaches the HDS−Si interface and results in the detachment of the MOF film. These results also indicate that film loss could be controlled by using low concentrations of the H_3BTC solution. Alternatively, limiting the reaction time before delamination occurs when thin HDS films are to be employed (based on Figure 5b) could also be effective for achieving densely covered thin (e.g., <100 nm) HKUST-1 films using HDS conversion.

CONCLUSION

We have demonstrated a custom-designed flow-cell ATR-FTIR system capable of probing surface reactions *in situ* during MOF thin film synthesis. This system was used to investigate the conversion of ZnO to (Zn,Cu) HDS and the subsequent conversion of HDS to HKUST-1 MOF at room temperature. Time-revolved spectra show that both ZnO-to-HDS and HDS-to-MOF reactions reach maximum conversion in <1 min. Combined experimental and modeling analyses reveal pseudo-first-order kinetics for each conversion step. The thickness of the HDS and the resulting MOF film product can be tuned by adjusting the thickness of ALD ZnO initial layers. We found that partial conversion of the initial ZnO film due to diffusion-limited reaction leads to an interfacial ZnO layer that can enhance the adhesion of the MOF film to the substrate. Our results provide important insights into the reaction conditions needed to produce surface-bound ultrathin MOF films. The flow reactor system with *in situ* ATR-FTIR described here is expected to aid the development and analysis of other thin film deposition processes, as well.

ASSOCIATED CONTENT

Supporting Information

The Supporting Information is available free of charge on the ACS Publications website at DOI: 10.1021/acs.chemmater.7b03096.

Experimental conditions, derivation of the ATR-FTIR kinetic model, schematic of the flow cell and optics, three-dimensional and contour plots of representative MOF growth experiments, optical and electron micrographs, X-ray diffraction patterns, and correlation between ATR and transmission FTIR (PDF)

AUTHOR INFORMATION

Corresponding Authors

*E-mail: gnp@ncsu.edu.

*E-mail: berc.kalanyan@nist.gov.

ORCID

Junjie Zhao: 0000-0001-6205-9671

Berc Kalanyan: 0000-0003-3508-9693

Gregory N. Parsons: 0000-0002-0048-5859

Author Contributions

J.Z. and B.K. contributed equally to this work.

Notes

The authors declare no competing financial interest.

ACKNOWLEDGMENTS

The authors acknowledge funding from ECBC (Grant W911SR-07-C-0075) and the Joint Science and Technology Office (Army Research Office Grant W911NF-13-1-0173). The authors thank Christopher Oldham for helping with the ALD processes. The authors also acknowledge the use of the Analytical Instrumentation Facility at North Carolina State University, supported by the State of North Carolina and the National Science Foundation.

REFERENCES

(1) Furukawa, H.; Cordova, K. E.; O'Keeffe, M.; Yaghi, O. M. The Chemistry and Applications of Metal-Organic Frameworks. *Science* **2013**, *341*, 1230444.

(2) Slater, A. G.; Cooper, A. I. Function-led design of new porous materials. *Science* **2015**, *348*, aaa8075.

(3) Li, J.-R.; Kuppler, R. J.; Zhou, H.-C. Selective gas adsorption and separation in metal-organic frameworks. *Chem. Soc. Rev.* **2009**, *38*, 1477−1504.

(4) Murray, L. J.; Dinca, M.; Long, J. R. Hydrogen storage in metal-organic frameworks. *Chem. Soc. Rev.* **2009**, *38*, 1294−1314.

(5) Lee, J.; Farha, O. K.; Roberts, J.; Scheidt, K. A.; Nguyen, S. T.; Hupp, J. T. Metal-organic framework materials as catalysts. *Chem. Soc. Rev.* **2009**, *38*, 1450−1459.

(6) Kreno, L. E.; Leong, K.; Farha, O. K.; Allendorf, M.; Van Duyne, R. P.; Hupp, J. T. Metal−Organic Framework Materials as Chemical Sensors. *Chem. Rev.* **2012**, *112*, 1105−1125.

(7) Sumida, K.; Rogow, D. L.; Mason, J. A.; McDonald, T. M.; Bloch, E. D.; Herm, Z. R.; Bae, T.-H.; Long, J. R. Carbon Dioxide Capture in Metal-Organic Frameworks. *Chem. Rev.* **2012**, *112*, 724−781.

(8) Walton, K. S. Inorganic chemistry: Movies of a growth mechanism. *Nature* **2015**, *523*, 535−536.

(9) Morris, R. E. How Does Your MOF Grow? *ChemPhysChem* **2009**, *10*, 327−329.

(10) Shoaee, M.; Anderson, M. W.; Attfield, M. P. Crystal Growth of the Nanoporous Metal−Organic Framework HKUST-1 Revealed by In Situ Atomic Force Microscopy. *Angew. Chem., Int. Ed.* **2008**, *47*, 8525−8528.

(11) Cubillas, P.; Anderson, M. W.; Attfield, M. P. Crystal Growth Mechanisms and Morphological Control of the Prototypical Metal−Organic Framework MOF-5 Revealed by Atomic Force Microscopy. *Chem. - Eur. J.* **2012**, *18*, 15406−15415.

(12) Shekhah, O.; Wang, H.; Zacher, D.; Fischer, R. A.; Wöll, C. Growth Mechanism of Metal−Organic Frameworks: Insights into the Nucleation by Employing a Step-by-Step Route. *Angew. Chem., Int. Ed.* **2009**, *48*, 5038−5041.

(13) Stavila, V.; Volponi, J.; Katzenmeyer, A. M.; Dixon, M. C.; Allendorf, M. D. Kinetics and mechanism of metal-organic framework thin film growth: systematic investigation of HKUST-1 deposition on QCM electrodes. *Chem. Sci.* **2012**, *3*, 1531−1540.

(14) Millange, F.; Medina, M. I.; Guillou, N.; Férey, G.; Golden, K. M.; Walton, R. I. Time-Resolved In Situ Diffraction Study of the Solvothermal Crystallization of Some Prototypical Metal−Organic Frameworks. *Angew. Chem., Int. Ed.* **2010**, *49*, 763−766.

DOI: 10.1021/acs.chemmater.7b03096
Chem. Mater. XXXX, XXX, XXX−XXX

(15) Wu, Y.; Moorhouse, S. J.; O'Hare, D. Time-Resolved in Situ Diffraction Reveals a Solid-State Rearrangement During Solvothermal MOF Synthesis. *Chem. Mater.* **2015**, *27*, 7236−7239.
(16) Cravillon, J.; Schröder, C. A.; Nayuk, R.; Gummel, J.; Huber, K.; Wiebcke, M. Fast nucleation and growth of ZIF-8 nanocrystals monitored by time-resolved in situ small-angle and wide-angle X-ray scattering. *Angew. Chem., Int. Ed.* **2011**, *50*, 8067−8071.
(17) Goesten, M.; Stavitski, E.; Pidko, E. A.; Gücüyener, C.; Boshuizen, B.; Ehrlich, S. N.; Hensen, E. J. M.; Kapteijn, F.; Gascon, J. The Molecular Pathway to ZIF-7 Microrods Revealed by In Situ Time-Resolved Small- and Wide-Angle X-Ray Scattering, Quick-Scanning Extended X-Ray Absorption Spectroscopy, and DFT Calculations. *Chem. - Eur. J.* **2013**, *19*, 7809−7816.
(18) Saha, S.; Springer, S.; Schweinefuß, M. E.; Pontoni, D.; Wiebcke, M.; Huber, K. Insight into Fast Nucleation and Growth of Zeolitic Imidazolate Framework-71 by In Situ Time-Resolved Light and X-ray Scattering Experiments. *Cryst. Growth Des.* **2016**, *16*, 2002−2010.
(19) Patterson, J. P.; Abellan, P.; Denny, M. S.; Park, C.; Browning, N. D.; Cohen, S. M.; Evans, J. E.; Gianneschi, N. C. Observing the Growth of Metal-Organic Frameworks by in Situ Liquid Cell Transmission Electron Microscopy. *J. Am. Chem. Soc.* **2015**, *137*, 7322−7328.
(20) Hind, A. R.; Bhargava, S. K.; McKinnon, A. At the solid/liquid interface: FTIR/ATR — the tool of choice. *Adv. Colloid Interface Sci.* **2001**, *93*, 91−114.
(21) Andanson, J.-M.; Baiker, A. Exploring catalytic solid/liquid interfaces by in situ attenuated total reflection infrared spectroscopy. *Chem. Soc. Rev.* **2010**, *39*, 4571−4584.
(22) Sabo, M.; Gross, J.; Wang, J.; Rosenberg, I. Performance Liquid-Chromatography Fourier-Transform Infrared Spectrometry with Normal and Reverse Phases Using an Attenuated Total Reflectance Flow Cell. *Anal. Chem.* **1985**, *57*, 1822−1826.
(23) Taga, K.; Kellner, R.; Kainz, U.; Sleytr, U. In-Situ Attenuated Total Reflectance Ft-Ir Analysis of an Enzyme-Modified Midinfrared Fiber Surface Using Crystalline Bacterial Surface-Proteins. *Anal. Chem.* **1994**, *66*, 35−39.
(24) Borda, M. J.; Strongin, D. R.; Schoonen, M. A. A novel vertical attenuated total reflectance photochemical flow-through reaction cell for Fourier transform infrared spectroscopy. *Spectrochim. Acta, Part A* **2003**, *59*, 1103−1106.
(25) Delille, A.; Quiles, F.; Humbert, F. In situ monitoring of the nascent Pseudomonas fluorescens Biofilm response to variations in the dissolved organic carbon level in low-nutrient water by attenuated total reflectance-fourier transform infrared spectroscopy. *Appl. Environ. Microbiol.* **2007**, *73*, 5782−5788.
(26) Schlenoff, J. B.; Rmaile, A. H.; Bucur, C. B. Hydration contributions to association in polyelectrolyte multilayers and complexes: Visualizing hydrophobicity. *J. Am. Chem. Soc.* **2008**, *130*, 13589−13597.
(27) Heinen, M.; Jusys, Z.; Behm, R. J. Ethanol, Acetaldehyde and Acetic Acid Adsorption/Electrooxidation on a Pt Thin Film Electrode under Continuous Electrolyte Flow: An in Situ ATR-FTIRS Flow Cell Study. *J. Phys. Chem. C* **2010**, *114*, 9850−9864.
(28) Lin, W.; Li, Z. Detection and Quantification of Trace Organic Contaminants in Water Using the FT-IR-Attenuated Total Reflectance Technique. *Anal. Chem.* **2010**, *82*, 505−515.
(29) Zhao, J.; Losego, M. D.; Lemaire, P. C.; Williams, P. S.; Gong, B.; Atanasov, S. E.; Blevins, T. M.; Oldham, C. J.; Walls, H. J.; Shepherd, S. D.; Browe, M. A.; Peterson, G. W.; Parsons, G. N. Highly Adsorptive, MOF-Functionalized Nonwoven Fiber Mats for Hazardous Gas Capture Enabled by Atomic Layer Deposition. *Adv. Mater. Interfaces* **2014**, *1*, 1400040.
(30) Khaletskaya, K.; Turner, S.; Tu, M.; Wannapaiboon, S.; Schneemann, A.; Meyer, R.; Ludwig, A.; Van Tendeloo, G.; Fischer, R. A. Self-Directed Localization of ZIF-8 Thin Film Formation by Conversion of ZnO Nanolayers. *Adv. Funct. Mater.* **2014**, *24*, 4804−4811.
(31) Zhao, J.; Gong, B.; Nunn, W. T.; Lemaire, P. C.; Stevens, E. C.; Sidi, F. I.; Williams, P. S.; Oldham, C. J.; Walls, H. J.; Shepherd, S. D.; Browe, M. A.; Peterson, G. W.; Losego, M. D.; Parsons, G. N. Conformal and highly adsorptive metal−organic framework thin films via layer-by-layer growth on ALD-coated fiber mats. *J. Mater. Chem. A* **2015**, *3*, 1458−1464.
(32) Zhao, Y.; Kornienko, N.; Liu, Z.; Zhu, C.; Asahina, S.; Kuo, T.-R.; Bao, W.; Xie, C.; Hexemer, A.; Terasaki, O.; Yang, P.; Yaghi, O. M. Mesoscopic constructs of ordered and oriented metal-organic frameworks on plasmonic silver nanocrystals. *J. Am. Chem. Soc.* **2015**, *137*, 2199−2202.
(33) Zhao, J.; Nunn, W. T.; Lemaire, P. C.; Lin, Y.; Dickey, M. D.; Oldham, C. J.; Walls, H. J.; Peterson, G. W.; Losego, M. D.; Parsons, G. N. Facile Conversion of Hydroxy Double Salts to Metal-Organic Frameworks Using Metal Oxide Particles and Atomic Layer Deposition Thin-Film Templates. *J. Am. Chem. Soc.* **2015**, *137*, 13756−13759.
(34) Lemaire, P. C.; Zhao, J.; Williams, P. S.; Walls, H. J.; Shepherd, S. D.; Losego, M. D.; Peterson, G. W.; Parsons, G. N. Copper Benzenetricarboxylate Metal−Organic Framework Nucleation Mechanisms on Metal Oxide Powders and Thin Films formed by Atomic Layer Deposition. *ACS Appl. Mater. Interfaces* **2016**, *8*, 9514−9522.
(35) Zhao, J.; Lee, D. T.; Yaga, R. W.; Hall, M. G.; Barton, H. F.; Woodward, I. R.; Oldham, C. J.; Walls, H. J.; Peterson, G. W.; Parsons, G. N. Ultra-Fast Degradation of Chemical Warfare Agents Using MOF-Nanofiber Kebabs. *Angew. Chem., Int. Ed.* **2016**, *55*, 13224−13228.
(36) Stassen, I.; Styles, M.; Grenci, G.; Gorp, H. V.; Vanderlinden, W.; Feyter, S. D.; Falcaro, P.; Vos, D. D.; Vereecken, P.; Ameloot, R. Chemical vapour deposition of zeolitic imidazolate framework thin films. *Nat. Mater.* **2016**, *15*, 304−310.
(37) Harrick, N. Electric Field Strengths at Totally Reflecting Interfaces. *J. Opt. Soc. Am.* **1965**, *55*, 851−857.
(38) Tompkins, H. G. The Physical Basis for Analysis of the Depth of Absorbing Species Using Internal Reflection Spectroscopy. *Appl. Spectrosc.* **1974**, *28*, 335−341.

DOI: 10.1021/acs.chemmater.7b03096
Chem. Mater. XXXX, XXX, XXX−XXX